An ancestral dual function of OmpM as outer membrane tether and nutrient uptake channel in diderm Firmicutes

Augustinas Silale[1], Yiling Zhu[1], Jerzy Witwinowski[2], Robert E. Smith[2], Kahlan E. Newman[3], Satya P. Bhamidimarri[1], Arnaud Baslé[1], Syma Khalid[4], Christophe Beloin[5], Simonetta Gribaldo[2], Bert van den Berg[1*]

[1] Biosciences Institute, Faculty of Medical Sciences, Newcastle University, Framlington Place, NE2 4HH, Newcastle upon Tyne, UK

[2] Institut Pasteur, Université de Paris Cité, UMR CNRS 6047, Unit Evolutionary Biology of the Microbial Cell, Paris, France

[3] School of Chemistry, University of Southampton, Southampton, SO17 1BJ, UK

[4] Department of Biochemistry, University of Oxford, Oxford, OX1 3QU, UK

[5] Institut Pasteur, Université de Paris Cité, UMR CNRS 6047, Genetics of Biofilms Laboratory, Paris, France

* Correspondence to: bert.van-den-berg@newcastle.ac.uk, simonetta.gribaldo@pasteur.fr, christophe.beloin@pasteur.fr

Abstract

The outer membrane (OM) in diderm, or Gram-negative, bacteria must be tethered to peptidoglycan (PG) for mechanical stability and to maintain cell morphology. Most diderm phyla from the Terrabacteria group lack well-characterised OM attachment systems such as Braun's lipoprotein, Pal and OmpA, but instead have the OmpM protein. OmpM has a periplasmic region containing an S-layer homology domain and a β-barrel region that is embedded in the OM. Here, we have determined the structure of the most abundant OmpM protein from the diderm firmicute *Veillonella parvula* by single particle cryogenic electron microscopy (cryo-EM). We reveal an OM portion similar to well-characterised trimeric general porins and a mobile periplasmic PG-binding region. Combining the cryo-EM data with crystal structures, structure predictions and molecular dynamics simulations, we show that the periplasmic region of OmpM likely adopts multiple conformations. Single-channel electrophysiology demonstrates ion conductance properties similar to *E. coli* OmpF. Finally, we demonstrate via functional assays that the four OmpM paralogues are likely to be the only general porins in *V. parvula*. Together, our results show that OM tethering and nutrient acquisition are genetically linked in *V. parvula* (and other diderm Firmicutes), suggesting that concurrent loss of two key OM-related functions, tethering and nutrient uptake, promoted the multiple OM loss events that have been inferred in the Terrabacteria.

Introduction

The defining feature of diderm, or Gram-negative, bacteria is the presence of an additional, outer membrane (OM)[1,2]. This complex cell envelope component is an asymmetric lipid bilayer, usually containing lipopolysaccharide (LPS) in the outer leaflet and phospholipids in the inner leaflet. The existence of an OM was first demonstrated by electron microscopy analysis of the cell envelope of the diderm Firmicute *Veillonella parvula*[3]. However, most of our knowledge about the OM derives from studies of Proteobacteria, especially *Escherichia coli*. While the OM provides mechanical stabilisation to the cell[4], diderm bacteria must tether the OM to peptidoglycan (PG) for additional mechanical stability and to maintain cell morphology. *E. coli* has three OM tethering systems: Braun's lipoprotein (Lpp) that covalently links the PG with the OM[5,6], the lipoprotein Pal and the OM protein OmpA which associate with PG non-covalently[7–11]. Mutants of these systems exhibit cell envelope defects and increased susceptibility to cell envelope stressors, such as detergents[7,12–15].

Recent phylogenetic analysis of the distribution of OM attachment systems throughout the bacterial tree of life has highlighted that the systems found in *E. coli* present a striking bimodal distribution across the two major clades in which Bacteria are divided, the Terrabacteria (including both monoderm and diderm phyla such as the Firmicutes and the Cyanobacteria, respectively) and the Gracilicutes (including only diderm phyla such as Proteobacteria and Bacteroidetes)[16]. Braun's lipoprotein is only present in a subset of Proteobacteria, and Pal is only present in Gracilicutes, together with the lipoprotein export (Lol) machinery. OmpA is also largely absent in many diderms. Strikingly, the OmpM protein is a fourth OM tethering system that is widespread in diderm Terrabacteria, but is completely absent in the Gracilicutes. OmpM consists of an N-terminal periplasmic S-layer homology (SLH) domain connected via a linker

region to a C-terminal OM β-barrel[17–20]. The SLH domain is expected to bind pyruvylated secondary cell wall polymers (SCWPs)[16,21–23], whereas *V. parvula* (and other members of the Negativicutes) anchor their OM to PG modified with polyamines (e.g. cadaverine and putrescine) on the D-glutamate of the peptide stem[18,24,25]. It is unclear why the Negativicutes apparently use a different ligand for OM anchoring, or whether the mechanism of attachment by OmpM is substantially different in this group. In both cases, the atomic details of PG binding to OmpM SLH domains are unclear.

Deletion of three out of the four OmpM paralogues in *V. parvula* resulted in a dramatic phenotype where the OM detaches, the periplasmic space is greatly enlarged and multiple cells share a single OM[16]. Complementation by the most abundant *V. parvula* OmpM paralogue, OmpM1, reverted this phenotype back to wild type. These data led to the proposal that OmpM proteins represent an ancestral OM tethering system in Terrabacteria and perhaps the last bacterial common ancestor, and might have been involved in multiple OM-loss events via OmpM mutations weakening (and eventually abolishing) the SLH-PG interactions.

Due to its LPS component, the OM presents a permeability barrier for hydrophilic and hydrophobic small molecules, both detrimental (*e.g.* antibiotics) and essential (*e.g.* nutrients)[26,27]. Controlled permeability of the OM is established by OM proteins, which either mediate energized transport of specific nutrients in the case of TonB-dependent transporters, or allow size-limited (<~600 Da) diffusion in the case of porins[26,27]. Porins are well-characterised in many Proteobacteria, but much less information is available on small-molecule permeation in diderm Terrabacteria. Earlier work on the OmpM orthologue Mep45 from the Negativicute *Selenomonas ruminantium* suggests that it can transport nutrients via its β-barrel domain[19], but another study on cyanobacterial

OM permeability suggests that its OmpM orthologues form a channel too small for most simple nutrientsa[20]. The role of OmpM in nutrient acquisition in *V. parvula* is unclear. In addition to the four OmpM paralogues, there are two other putative porin genes in the *V. parvula* genome: an OmpA-like homologue (*FNLLGLLA_00518*) and a sixth porin (*FNLLGLLA_00833*)[28]. Proteomic analysis of the *V. parvula* OM showed that OmpM1, OmpM2 and FNLLGLLA_00833 are, respectively, the first, third, and sixth most abundant OM proteins[28], suggesting that these proteins could play major roles in determining OM permeability.

A recent analysis has suggested that the barrels of most OmpM-like proteins have 16-30 β–strands[29], and could therefore form pores that are large enough for small molecule diffusion across the OM, a hypothesis supported by electrophysiology experiments with the diderm Terrabacterium *Deinococcus radiodurans* SlpA protein[30] and liposome swelling studies on Mep45 from *S. ruminantium*[19]. The recently determined structures of SlpA reveal that it forms a very large trimeric complex composed of 30-stranded β-barrels, *i.e*. much larger than those of the general *E. coli* porins OmpC and OmpF[29,30]. In any case, it is unclear how generalisable the findings are from SlpA of *D. radiodurans*, which has an unusually complex cell envelope with an S-layer[31–33], to OmpM proteins in other diderm Terrabacteria, especially in Negativicutes which tether the OM to polyaminated PG rather than pyruvylated SCWP.

Here we use single particle cryo-EM, X-ray crystallography, molecular dynamics simulations, bioinformatic analyses and functional assays to show that OmpM1 from *V. parvula* (VpOmpM1) is a general porin with similar structural and functional properties to *E. coli* OmpF, and an additional mobile periplasmic region that can take

on different folds. We also show that the four OmpM paralogues are likely the only porins in *V. parvula*, implying that nutrient acquisition and OM attachment are genetically linked in diderm Firmicutes, and likely all diderm Terrabacteria, via OmpM. Our results support an ancestral dual function of OmpM as both an OM tether and nutrient uptake porin which may have supported life in early bacteria.

Results

VpOmpM1 is a trimeric porin with an extended periplasmic region

We determined the structure of VpOmpM1 expressed in *E. coli* by single particle cryo-EM (Figure 1a-c and Supplementary Table 1). Reconstructions up to 3.2 Å without enforced symmetry revealed a trimeric arrangement of the protomers. The C-terminal 16-stranded β-barrels that reside in the OM form a classical three-fold symmetrical porin trimer reminiscent of the well-characterised *E. coli* porins OmpF (EcOmpF) and OmpC[34,35]. However, the β-barrel lumens are constricted by inward-folded extracellular loops 3 and 7 in VpOmpM1 (Figure 1b), rather than solely by loop 3 as in the *E. coli* porins. The inter-protomer contact area, mediated by hydrophobic sidechains on the outside of the β-barrel, completely excludes lipid/detergent and solvent. The β-barrels exhibit other features common to known porin structures, including an aromatic girdle at the putative membrane-solvent interfaces and strong density surrounding the β-barrels that likely corresponds to the lipid moieties of LPS and phospholipid or detergent (Figure 1b, c and Supplementary Figure 1).

An unusual feature observed in the cryo-EM reconstructions was a weaker, elongated density that corresponds to the N-terminal SLH domain at the distal part, connected to the β-barrel via a triple coiled-coil (Figure 1c, d). We term this periplasmic region of VpOmpM1 the ‘stalk’. Only the region of the stalk proximal to the OM was resolved

well enough for model building, as the cryo-EM density deteriorates towards the SLH domain end of the stalk. We speculated that the poor density is the result of movement of the stalk relative to the β-barrels. Measurements of the blurry SLH domain density observed in 2D class averages suggest that the distal part of the stalk spans 50-60 Å (Figure 1d). The VpOmpM1 trimer is pseudosymmetrical: while the β-barrels exhibit three-fold symmetry, the stalk is tilted relative to the membrane plane normal (Figure 1c). The pseudosymmetry was confirmed by enforcing C3 symmetry during data processing, which resulted in a better-resolved β-barrel region (2.8 Å) but uninterpretable density for the periplasmic stalk (Supplementary Figure 2).

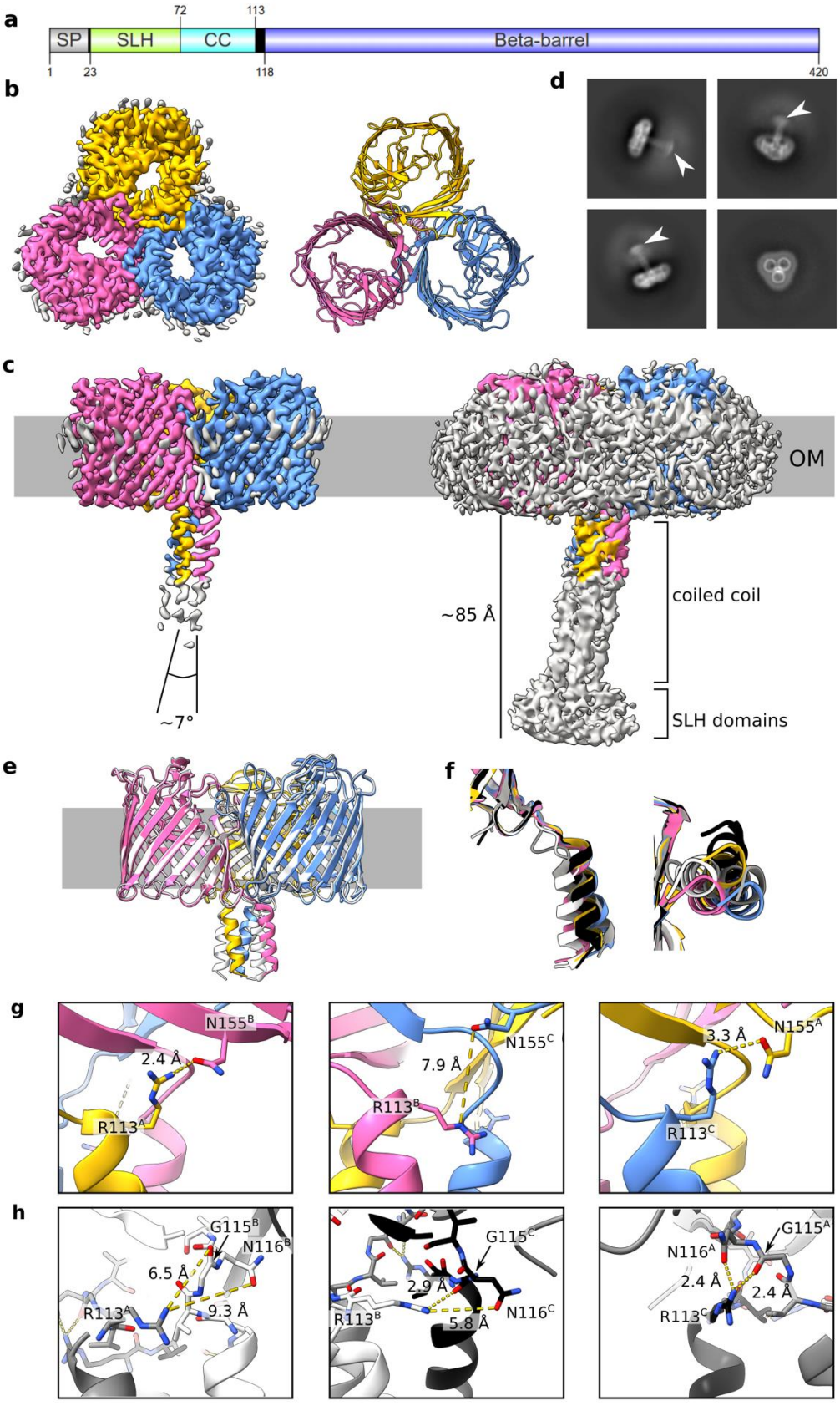

159

160 **Figure 1. Cryo-EM structures of VpOmpM1 expressed in *E. coli* and *V. parvula*. a**
161 Schematic depicting VpOmpM1 (UniProt A0A100YN03) domain arrangement and
162 boundaries. SP, signal peptide; SLH, S-layer homology; CC, coiled coil. Generated using IBS
163 2.0 [36]. **b** Structure of recombinant VpOmpM1. The cryo-EM density is shown on the left and

the model is shown on the right as viewed towards the OM from outside the cell. **c** Side view of the cryo-EM density at high (left) and low (right) contour. The grey bar represents the outer membrane (OM). The diffuse grey density around the membrane region in the high contour view likely corresponds to lipid or detergent. **d** Representative 2D class averages. White arrowheads point to the diffuse SLH domain density. The edge of each square is 344.4 Å long. **e** Superposition of structures from recombinant VpOmpM1 (in colour) and native VpOmpM1 purified from *V. parvula* (white). **f** Superposition of protomers from the recombinant (yellow, pink, blue) and native (grey, white, black) VpOmpM1 structures. The structural alignment was performed on the β-barrel region only (not shown). Left – side view, right – view from the periplasm towards the OM. **g, h** Inter-protomer contacts at the β-barrel-stalk interface in the recombinant (**g**) and native (**h**) structures. The protomer (A, B, C) for each sidechain is indicated in superscript.

The *E. coli* cell wall does not contain polyaminated PG, the native ligand of VpOmpM1. Therefore, to exclude the possibility that in our structure of VpOmpM1 purified from *E. coli* the stalk region is misfolded due to the absence of polyaminated PG, we purified a His-tagged OmpM1 construct expressed in *V. parvula* (native VpOmpM1) and determined its structure by single particle cryo-EM to 3.3 Å resolution (Supplementary Table 1). The β-barrel structures are virtually identical (Cα-Cα root-mean-square deviation 0.239 Å), but there are differences in the relative orientation of the stalk (Figure 1e). In reconstructions without enforced symmetry, the α-helices forming the coiled-coil are not equivalent in either dataset, as they exit the OM plane in different orientations (Figure 1f). The reasons for these structural differences are not obvious. We speculated that intra- or inter-protomer hydrogen bonds at the stalk-barrel interface could be responsible for the subtle conformational differences. In the *E. coli* VpOmpM1 structure, the sidechain of R113 in one protomer interacts with the sidechain of N155 (part of the periplasmic end of the β2 strand) of another protomer. This interaction is observed only in two inter-protomer interfaces, but not the third one (Figure 1g). A similar interaction was observed in the native VpOmpM1 structure: at two inter-protomer interfaces, R113 interacts with the carbonyl oxygen of G115 and the sidechain of N116 (both part of the β-barrel end of the stalk) (Figure 1h). Interestingly, the R113-N155 interaction was not observed in the native VpOmpM1

196 structure, and the R113-G115/N116 interaction was not observed in the VpOmpM1
197 structure from *E. coli*. It is possible that the two constructs differ slightly in their lowest
198 energy states which are observed in the averaged cryo-EM data.
199
200 We performed all-atom molecular dynamics (MD) simulations to investigate the
201 conformational space sampled by the stalk. We simulated the native VpOmpM1 model
202 to which an AlphaFold2[37] prediction of the unmodeled region of the stalk was grafted
203 and fit into the low resolution cryo-EM density (Figure 2a). The simulations revealed
204 substantial movement of the stalk in the periplasmic space (Supplementary Movie 1).
205 The SLH domain end of the stalk sampled a span of ~50 Å (Figure 2b) during the
206 simulations, in agreement with the cryo-EM data (Figure 1d). The coiled-coil does not
207 kink throughout the 1 μs simulation (Figure 2c), and the movement of the stalk is due
208 to flexibility at the interface between the stalk and the β-barrels. We observed that the
209 inter-protomer hydrogen bonds identified in our static cryo-EM structures, R113-N155
210 and R113-G115, are broken and re-formed throughout the simulation (Figure 2d). The
211 R113 interaction with the sidechain of N116 was not stable, and R113 instead
212 interacted with the backbone carbonyl oxygen of N116 (Figure 2d). Similar results
213 were obtained from a replicate simulation with the AlphaFold2 graft model as well as
214 the native VpOmpM1 cryo-EM model by itself (Supplementary Figure 3). The stalk
215 would presumably be bound to the relatively immobile PG in vivo, which would
216 significantly impair its mobility relative to the OM. We speculate that the flexible
217 interface between the stalk and the β-barrels would result in the ability of the OM to
218 move slightly relative to the PG, imparting mechanical resistance to the cell envelope.
219

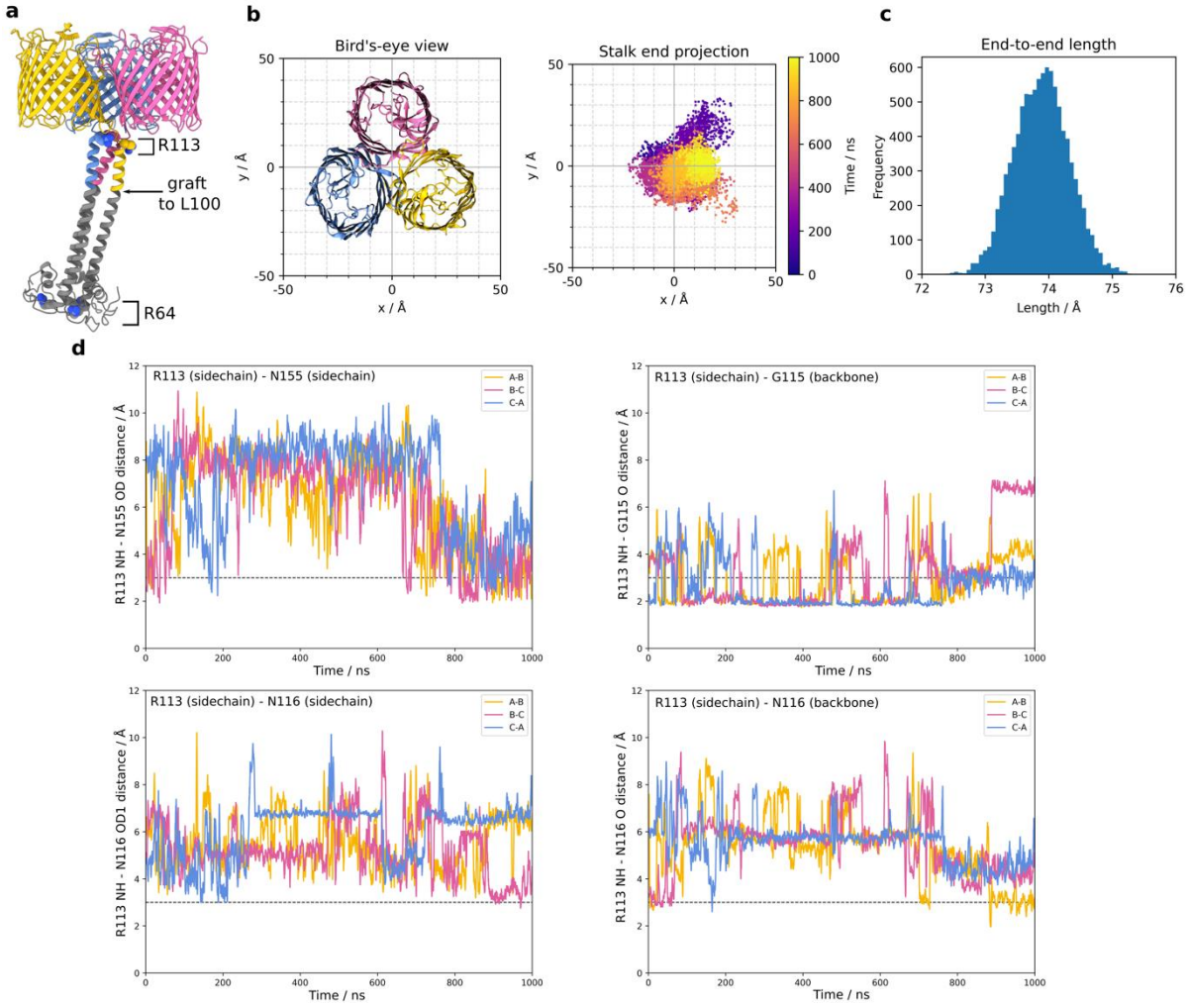

Figure 2. All-atom molecular dynamics simulations with native VpOmpM1. **a** The AlphaFold2 prediction for the stalk (grey) was grafted onto the N-terminus of the first residue (L100) modelled into the experimental density of native VpOmpM1 (in colour). R64 (bottom of SLH domain) and R113 are shown as space filling models. **b** Bird's-eye-view of the β-barrel region from outside the OM (left) and a plot of the stalk end projection (centre of mass of the R64 Cα atoms) over the 1 μs simulation (right). The observation point in the left and right panels is equivalent. **c** Frequency distribution of stalk lengths (R64-R113 Cα-Cα) observed throughout the simulation. **d** Distances between the R113 sidechain and interacting sidechain atoms throughout the simulation. The dotted line denotes an inter-atomic distance of 3 Å. The equivalent plots for a replicate simulation and a simulation without the AlphaFold2 graft are presented in Supplementary Figure 3.

Polyaminated PG is potentially recognised by conserved tyrosine residues

The SLH domain of OmpM binds polyaminated PG *in vivo*, as demonstrated in *V. parvula* (Kamio & Nakamura, 1987) and *S. ruminantium*[18,24]. The cryo-EM density for VpOmpM1 SLH domains was not sufficiently resolved for model building due to movement of the stalk, as demonstrated by MD simulations. We used bioinformatics and structural comparisons to investigate where polyaminated PG could bind within

the AlphaFold2 predicted model of VpOmpM1 SLH domains. Monoderm bacteria attach cell surface proteins to SCWPs via triple tandem SLH domain repeats in a single protein chain, which fold into a core three α-helix bundle with additional helices and loops packing against this bundle[38–42]. Crystal structures of the SLH domains 1-3 of *Bacillus anthracis* surface array protein (Sap) and *Paenibacillus alvei* S-layer protein SpaA are similar to the predicted VpOmpM1 SLH domain[39,40] (Figure 3a) with Cα-Cα r.m.s.d values of 1.0 and 1.3 Å, respectively. The main difference is that both Sap and SpaA have short core helical bundles, but the VpOmpM1 central bundle extends into the long coiled-coil that connects it to the β-barrels. Structures of SpaA bound to defined SCWP ligands show that the sugars bind in grooves between SLH repeats (Figure 3a) and interact with conserved motifs therein: conserved tryptophan and glycine residues bind the sugar moiety (W34 and G58 in VpOmpM1), and the arginine of the TRAE motif forms a salt bridge with the ketal-pyruvate modification of the SCWP (residues 63-66, TRYE, in VpOmpM1). It is not surprising that these motifs are conserved in OmpM (Figure 3b and c) because most OmpM-like proteins from Terrabacteria other than the Negativicutes are thought to bind pyruvylated SCWP.

Negativicute OmpM proteins are thought to recognise the polyamine modification on the α-carboxylate of the D-glutamate in the PG peptide stem. Crystal structures of proteins bound to putrescine[43–45] and cadaverine[46,47] indicate that aromatic residues are involved in binding these polyamines via stacking interactions with the aliphatic chain of the polyamine. We compared subsets of OmpM SLH domain sequences from all Terrabacteria either excluding the Firmicutes, or from only the Firmicutes, or from only the Negativicutes to non-OmpM SLH domain sequences from the Firmicutes. We found that the tyrosine residue Y36 is highly conserved in the Negativicutes, slightly less conserved within the Firmicutes, and not conserved in OmpM homologues from

other phyla and non-OmpM SLH domains (Figure 3b and c). Also, Y65 of the TRYE motif is more conserved in the Negativicutes than in other groups. Mapping the conserved residues onto the predicted VpOmpM1 SLH domain structure reveals that the conserved tyrosines are located away from the grooves between the SLH chains that contain the putative PG disaccharide binding site (Figure 3d). We suggest that the peptide stem containing the polyamine moiety could extend away from the disaccharide binding groove to interact with either of the conserved tyrosines. Alternatively, or perhaps additionally, PG interaction could induce conformational changes that bring the tyrosine side chains closer to the binding groove. These possibilities will have to be further investigated by binding studies and by determining structures of the SLH domain with purified PG fragments.

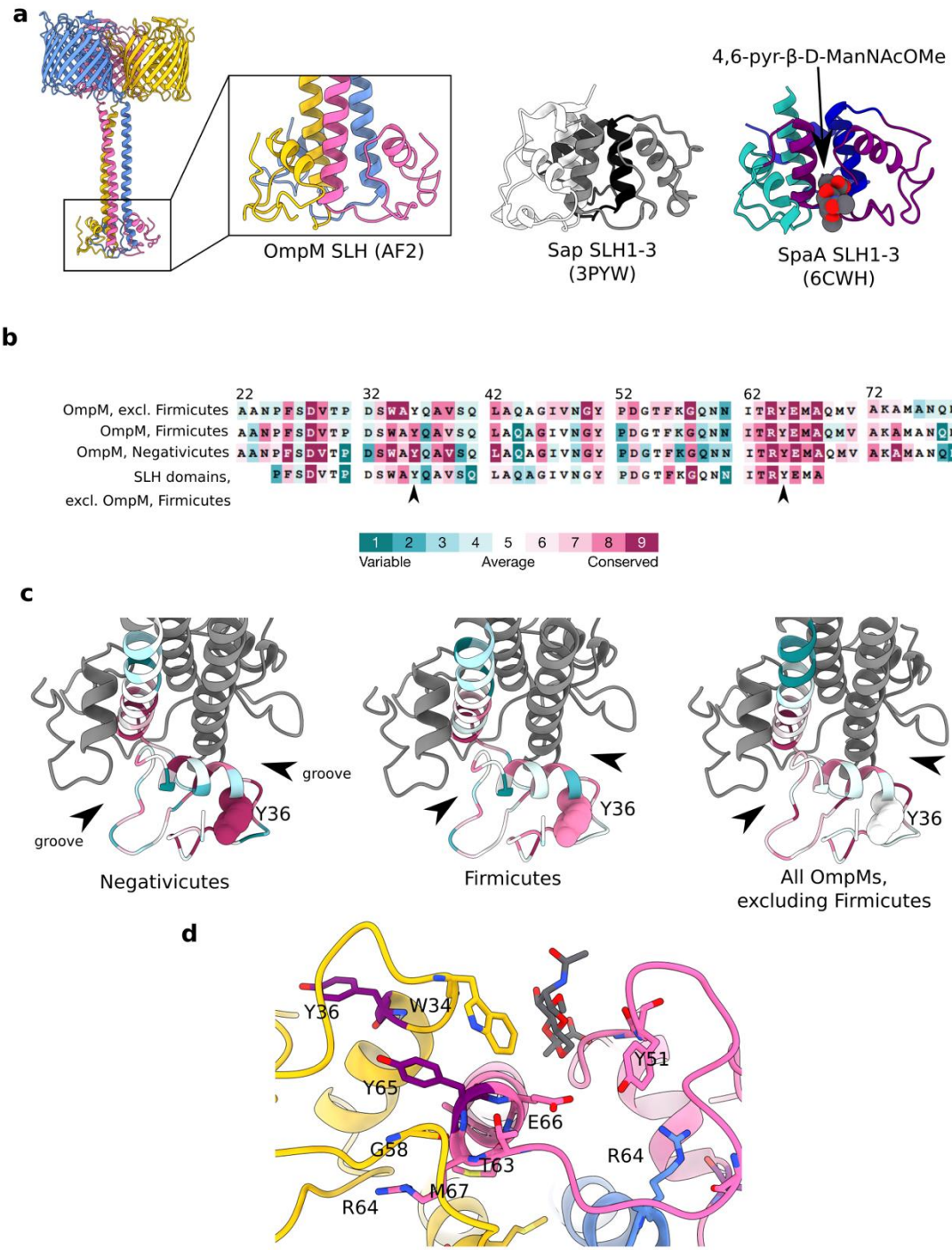

Figure 3. Analysis of the putative peptidoglycan binding site within the SLH domain. a Close up view of the VparOmpM1 SLH domains predicted by AlphaFold2, the crystal structure of SLH domains 1-3 from *Bacillus anthracis* Sap (surface array protein) (PDB 3PYW)[39], and the crystal structure of SLH domains 1-3 from *Paenibacillus alvei* SpaA in complex with the monosaccharide 4,6-pyr-β-D-ManNAcOMe (space-filling representation) (PDB 6CWH) [40]. Views were generated from a superposition. **b** Multiple sequence alignment results from different subsets of SLH domain-containing proteins mapped onto the sequence of VpOmM1 SLH domain and coloured by conservation using ConSurf [48] (colour key). Row 1 - representative OmpM homologues from across the Terrabacteria, except the Firmicutes (211 sequences); row 2 – representative OmpM homologues from all diderm Firmicutes (67 sequences); row 3 – OmpM homologues from Negativicutes (615 sequences); row 4 – SLH domains from proteins other than OmpM found in all Firmicutes (60 sequences). The arrows

point to Y36 and Y65, which could be important for binding polyaminated PG. **c** ConSurf results mapped onto the predicted SLH domains of VpOmpM1 (same sequence subsets and colour key as **b**). Arrows point to the grooves between SLH protomers. Y36 is shown in space-filling representation. The datasets used for ConSurf analysis correspond to the datasets used in a previous study[16] that were subsampled using custom scripts. **d** Conserved residues shown as stick models on the predicted SLH structure, coloured by chain, except for Y36 and Y65 which are in purple. SpaA bound to monosaccharide (PDB 6CWH) was superposed onto the VpOmpM1 SLH structure; the monosaccharide is in grey, the SpaA protein model is not shown.

We generated a soluble construct encompassing almost the entire VpOmpM1 stalk region (residues 22-107) in *E. coli* and determined its crystal structure to 1.7 Å (Figure 4a, Supplementary Table 2) in an attempt to verify the AlphaFold2 prediction for this region. Surprisingly, the crystallized stalk does not fold into a coiled-coil but forms a compact trimer composed mainly of α-helical bundles (residues 23-105). The protomer interfaces form grooves on one side of the trimer that could potentially accommodate ligands (Figure 4b). However, mapping of putative PG-binding residues onto the stalk crystal structure shows they are spread across the structure (Supplementary Figure 4), suggesting that this conformation of the stalk does not bind PG. The residues that form the coiled-coil in the extended AlphaFold2 prediction instead form helical hairpins and extensive intra-protomer interactions rather than interact with the other chains in the asymmetric unit (Figure 4c). We obtained a very similar structure, albeit at a lower resolution, with a longer construct that encompasses the entire stalk region (residues 22-118). A DALI[49] search of the PDB using these models showed that the SLH domain crystal structure has low structural similarity to other proteins (Supplementary Figure 5).

The protomer fold of the stalk observed in the crystal structures aligns well with an alternative, compact conformation predicted by AlphaFold2 (Figure 4d and e, Supplementary Figure 6). This was also surprising as the confidence for this prediction was low, yet it agreed with the experimental structure. However, the trimerization

interface in the compact stalk prediction is different: residues that are far away in the crystal structure (e.g. M75) interact in the predicted compact conformation (Figure 3e). We hypothesised that this compact state could be an unstable high energy conformation (hence the low prediction confidence), and that the stalk construct is stabilized in a similar high energy conformation in the crystallization condition. All-atom MD simulation of VpOmpM1 with the compact stalk showed the stalk helix of one protomer reaching towards the OM, partially occluding the β-barrel of another protomer and forming salt bridges with its periplasmic turns (Figure 4f and Supplementary Movie 2). Additionally, this conformation was stabilised by inter-protomer hydrogen bonds in the stalk region (Supplementary Figure 7). The role of this interaction is unclear, but this simulation supports the dynamic nature of the stalk.

The two strikingly different stalk conformations of VpOmpM1 imply that either there is conformational switching under the appropriate conditions (e.g. cell envelope stress, presence of specific ligands), or that the protein is committed to a particular conformation during biogenesis. In one replicate of the all-atom MD simulations of the native VpOmpM1-AlphaFold2 graft model (Figure 2a) we observed unfolding of the very N-terminus of the SLH domain of one chain, which then proceeded to interact with residues of the coiled-coil (Supplementary Movie 3, Supplementary Figure 8). This suggests some flexibility for the SLH domain, and perhaps *in vivo* this flexibility is important for the SLH domain to find its PG ligand. The coiled-coil, however, remained stable during the simulation. Protein melting temperature analysis by dynamic scanning calorimetry suggested that the melting temperature of the stalk in the full-length VpOmpM1 construct is ~87˚C (Supplementary Figure 9), which means that the coiled-coil interaction is very stable and is unlikely to unfold under physiological conditions. Therefore, the more favourable hypothesis is that the

345 VpOmpM1 trimer is committed to either the extended or compact stalk conformation
346 during biogenesis.

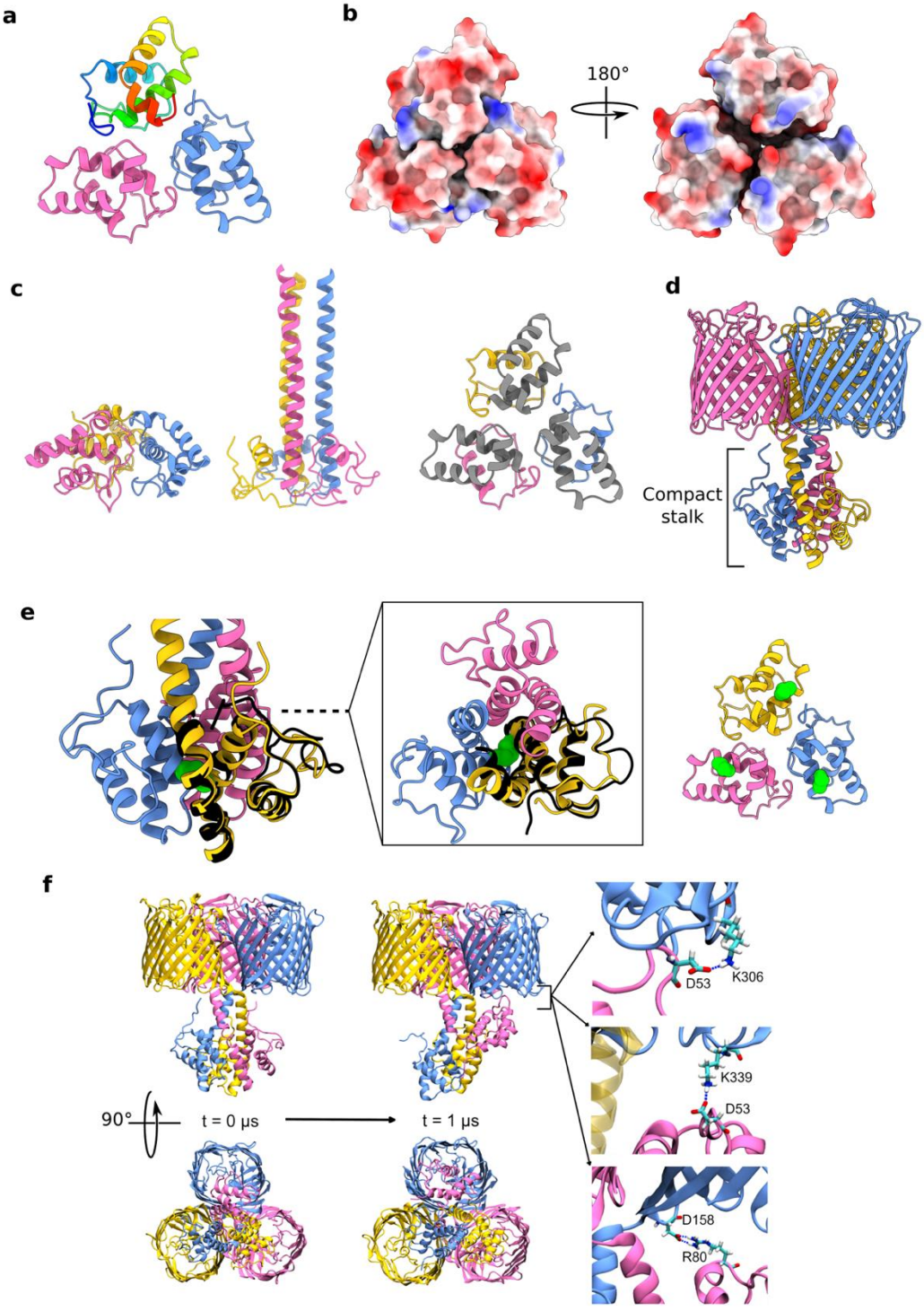

347

348 **Figure 4. Crystallography and AlphaFold2 show evidence of alternate stalk**
349 **conformations. a** Crystal structure of VpOmpM1 stalk trimer at 1.7 Å. Residues 23-105 were
350 resolved. One chain is in rainbow: N-terminus is blue, C-terminus is red. **b** Electrostatic surface
351 presentation of the stalk crystal structure. (Left) Putative view from the OM and (right) from
352 the periplasm. **c** Comparison of the stalk crystal structure (left) and AlphaFold2 predicted
353 extended conformation (middle). Only residues 23-105 are displayed for both. (Right)

Residues 64-105 of the stalk crystal structure that form the extended coiled-coil in the AlphaFold2 prediction are in grey. **d** Alternative, compact stalk conformation predicted by AlphaFold2. **e** Close up view of the compact stalk prediction with a single chain from the crystal structure (black) superposed (Cα-Cα r.m.s.d. 0.78 Å) (left). (Middle) Top view down the section marked by the dashed line. (Right) Stalk crystal structure. The sidechain of M75 is shown in green space-filling representation in each panel. **f** All-atom MD simulation of AlphaFold2 predicted compact stalk model over 1 μs. The SLH domain of one of the protomers (pink) reaches towards the OM and interacts with the periplasmic turns of the β-barrel of another protomer (blue). The salt bridges shown on the right had occupancies of 5.8%, 3.44% and 1.89% (top to bottom) throughout the simulation.

OmpM paralogues are the only general diffusion porins in *V. parvula*

The β-barrel of VpOmpM1 consists of 16 anti-parallel β-strands connected by extracellular loops and periplasmic turns (Figure 1b,c). The overall structure is similar to EcOmpF, and the differences lie in the extracellular loops (Figure 5a and Supplementary Figure 10). VpOmpM1 extracellular loops 3 and 7 fold into the β-barrel to form the constriction. In EcOmpF and similar Proteobacterial general porins the constriction is formed solely by loop 3 (Figure 5a). The eyelet (the narrowest region of the pore) is formed by sidechains projecting from the β-barrel strands into the lumen as well as sidechain and backbone atoms of the constricting loop residues (Figure 5b). It is thought that an electric field exists across the eyelet of EcOmpF as a result of asymmetric distribution of charged residues[50,51], and a similar charge asymmetry is seen in the eyelet of VpOmpM1 (Figure 5b). Analysis of the pore radius of both β-barrels by the HOLE program[52] reveals a maximal constriction of ~3.7 Å (Figure 5c). However, in EcOmpF the extent of the constriction (±0.1 Å) along the axis perpendicular to the membrane plane is ~2.4 Å, and the VpOmpM1 constriction extends for ~7 Å.

We tested the potential of VpOmpM1 to transport small molecules across membranes in liposome swelling assays (Figure 5d). Notably, VpOmpM1 could transport lactate, which is essential for *V. parvula* growth, and putrescine, which is used for modification

386 of the PG peptide stem. We also observed transport of the amino acids arginine,
387 lysine, glutamate, aspartate, glycine, alanine, leucine, and methionine. VpOmpM1
388 transported monosaccharides, even though *V. parvula* is asaccharolytic, but not
389 disaccharides, which underlines the non-specific, size-limited nature of the transport
390 activity. We carried out experiments with a VpOmpM1 construct that lacks the stalk to
391 test if the stalk is involved in regulating transport, but this construct had similar
392 transport properties to the full-length protein (Figure 5d). The only exception was
393 impaired transport of arginine and alanine, and the reasons for this are unclear.
394 VpOmpM1 had a similar substrate permeation profile to EcOmpF but showed
395 consistently lower transport rates, which could be the consequence of a longer
396 constriction region and the presence of additional charges in the eyelet (Figure 5b, c).
397 One notable difference is that there was little transport of ampicillin, kanamycin and
398 gentamicin by VpOmpM1 compared to EcOmpF (Figure 5d), but the relevance of this
399 for antibiotic resistance *in vivo* is unclear.
400
401 We further characterised the channel properties of VpOmpM1 in bilayer
402 electrophysiology experiments. Initially, we obtained conductance value distributions
403 from recordings with multiple channel insertion events (Figure 5e and Supplementary
404 Figure 11a,b). The resulting distributions were very broad and centred at 4.87 ± 1.86
405 nS and 4.66 ± 1.88 nS for the full-length and barrel-only constructs of VpOmpM1,
406 respectively. The broad conductance distributions are likely due to multiple sub-
407 conductance states of the channel, as observed in recordings where the channels can
408 randomly close to different extent (Figure 5f and Supplementary Figure 11c,d). We
409 were able to get more accurate conductance values from single channel recordings:
410 4.34 ± 0.46 nS (s.d., n=8) for full-length VpOmpM1 and 4.37 ± 0.28 nS (s.d., n=8) for
411 barrel-only VpOmpM1. In single channel recordings at higher voltages, we

occasionally observed classical trimeric porin behaviour where the three protomer pores close sequentially (Figure 5f and Supplementary Figure 11c,d). Using our setup we obtained a conductance of 4.28 ± 0.19 (s.d., n=9) for EcOmpF, which is similar to previously reported values[53,54] and to VpOmpM1 conductance. Current-voltage characteristics for both VpOmpM1 constructs and EcOmpF were again very similar (Figure 5g).

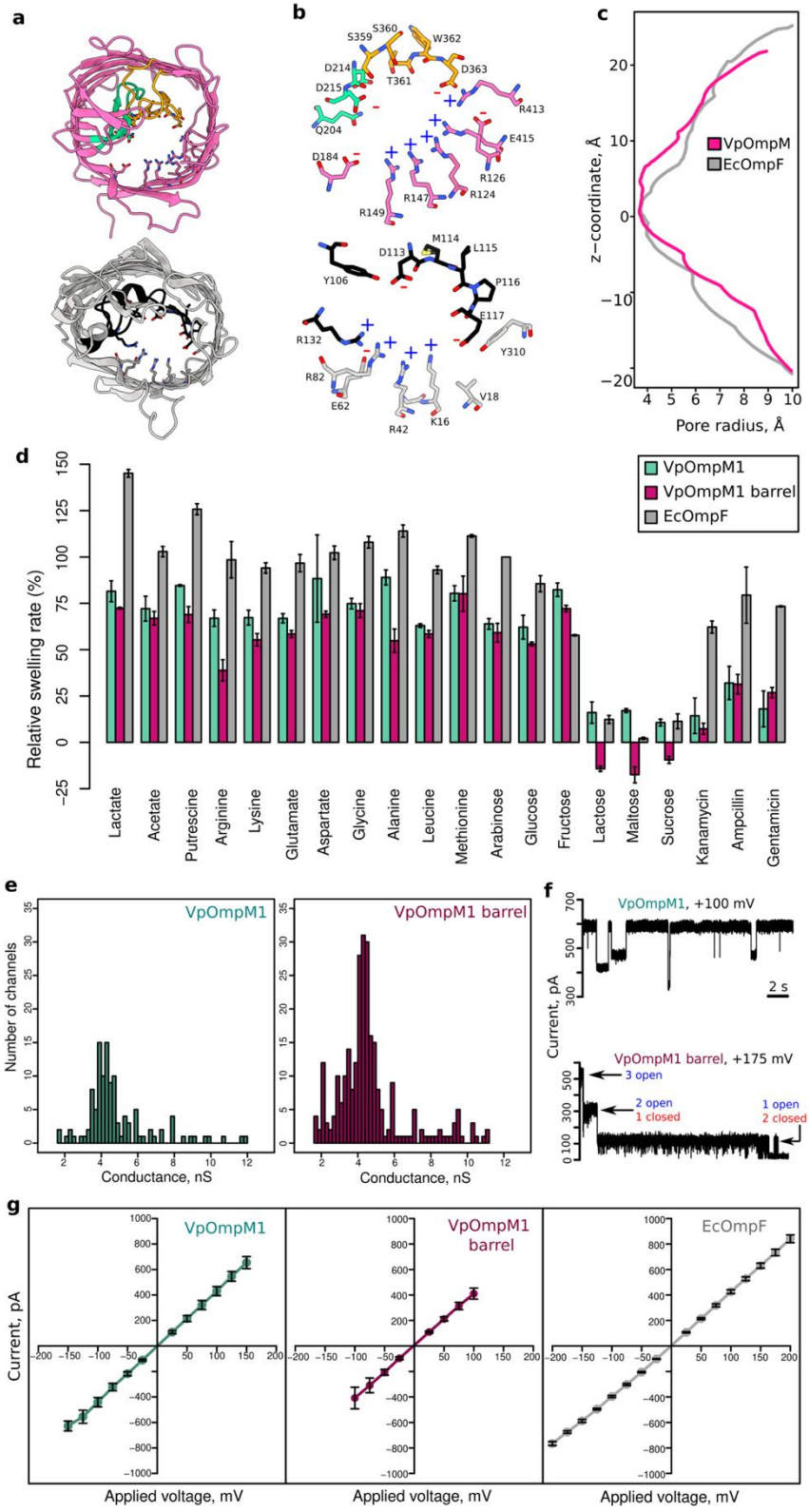

Figure 5. VpOmpM1 has general diffusion channel properties. **a** β-barrel from the C3 cryo-EM reconstruction of VpOmpM1 (top) and an EcOmpF protomer (PDB 3POQ)[55] (bottom). The views are generated from a superposition. VpOmpM1 loops 3 and 7 are in green and orange, respectively; EcOmpF loop 3 is in black. Residues forming the eyelet are shown in stick representation. **b** Close-up view of the eyelet regions of VpOmpM1 (top) and EcOmpF (bottom). Colours as in **a**. Positively and negatively charged residues lining the eyelet are annotated with a blue plus or red minus sign, respectively. **c** HOLE[52] profile of VpOmpM1 and

EcOmpF. The z-coordinate is perpendicular to the membrane plane and its origin is at the narrowest part of the VpOmpM1 eyelet. **d** Liposome swelling in the presence of indicated substrate. Liposomes with embedded full-length VpOmpM1, VpOmpM1 barrel-only or EcOmpF were tested. Swelling rates were normalised to the rate of swelling of EcOmpF-containing liposomes in the presence of arabinose. Each condition was measured in technical triplicates from the same liposome preparation. Error bars show ± s.d. **e** Bilayer electrophysiology conductance distribution plots obtained from recordings with multiple insertion events (see Supplementary Figure 11a for representative traces). Full-length VpOmpM1 distribution is centred on 4.87 ± 1.86 nS (s.d., n=117); VpOmpM1 barrel-only distribution is centred on 4.66 ± 1.88 nS (s.d., n=269). **f** Representative bilayer electrophysiology recordings of full-length VpOmpM1 (top) showing multiple sub-conductance states and of the barrel-only construct (bottom) showing classical trimeric porin sequential channel closure at high voltage. **g** Current-voltage characteristics from single channel recordings of full-length VpOmpM1, barrel-only VpOmpM1 and EcOmpF. Data from at least three channel recordings were used at each applied voltage.

We conclude that VpOmpM1 is a general diffusion channel in *V. parvula*, with similar properties to EcOmpF. We expect that the VpOmpM2-4 paralogues also function as nutrient uptake channels based on their sequence similarity[16]. We think it unlikely that the other two putative porins of *V. parvula*, FNLLGLLA_00518 (OmpA-like) and FNLLGLLA_00833, also transport nutrients because they are predicted to only have 10 strands in their β-barrels (Figure 6a,b). Previous work on 10-stranded β-barrels has shown that their lumen is occluded by amino acid residue sidechains and that they cannot perform major transport roles[56,57], and we wanted to verify this experimentally. We could produce the β-barrel region of FNLLGLLA_00518 in sufficient quantities for liposome swelling experiments. It did not transport lactate and arabinose, and could only transport putrescine and glycine at much slower rates than VpOmpM1 and EcOmpF (Figure 6c), in agreement with reported transport properties of small OM β-barrels[58,59]. Therefore, FNLLGLLA_00518 is not a general porin. We were not able to test the transport activity of FNLLGLLA_00833 because the protein could not be expressed in *E. coli*, but we expect this 10 β-stranded OM protein to have very low substrate permeation rates as well.

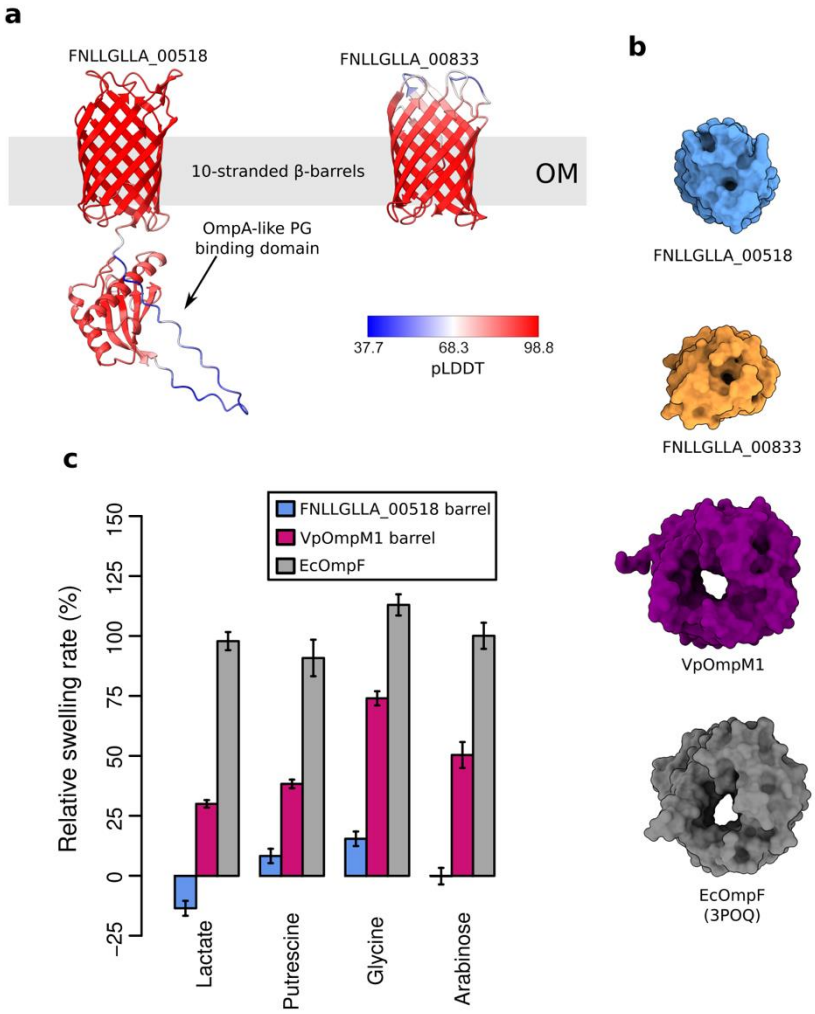

459

460 **Figure 6. *V. parvula* OM proteins other than OmpM paralogues are unlikely to be general**
461 **diffusion channels. a** AlphaFold2[37] models of the FNLLGLLA_00518 (OmpA-like) and
462 FNLLGLLA_00833 proteins. The colours represent the per residue confidence of the
463 prediction (pLDDT). **b** Molecular surface models of *V. parvula* OM proteins and EcOmpF as
464 viewed from outside the cell. **c** Comparative liposome swelling assays with FNLLGLLA_00518
465 β-barrel, VpOmpM1 β-barrel, and EcOmpF.

466

467

Discussion

Together, our results show that OmpM has a dual function as an OM tethering system and a nutrient uptake channel. Our structures, simulations and functional data provide insight into how these key OM-related functions are linked in the diderm Firmicutes and probably many other diderm bacteria that lack the well-characterised OM attachment systems present in the Gracilicutes.

Interestingly, structural data and MD simulations show that the extended stalk of VpOmpM1 is highly mobile. The functional consequences of this mobility are not clear, and neither is it clear why it is preferable to a rigid connection between the PG and OM. One possibility is that the stalk samples the local environment to find polyaminated-PG. Although one would expect the polyamine modification to be present on most peptide stems, PG spatial organization is not well understood, and it is unclear what proportion of the modified peptide stems is easily accessible to the SLH domains of VpOmpM1. Another possibility is that the flexible interface between the stalk and the β-barrels imparts favourable mechanical properties to the cell envelope, as having a somewhat flexible PG-OM tether would allow the OM to deform slightly when external mechanical forces are applied.

Using an integrative approach, we have shown that VpOmpM1 might exist in multiple conformations, despite the fact we did not observe any particle populations with a compact stalk in our cryo-EM datasets. Unravelling the roles of both potential states of the stalk is a challenging problem that will likely have to be resolved using *in vivo* studies. We expect that the extended stalk state observed in cryo-EM reconstructions is the PG-binding state based on structural comparisons with SCWP-binding SLH domains from monoderm bacteria. However, we cannot exclude that both states are

competent to bind PG. Additionally, the VpOmpM1 stalk represents a newly identified variation on SLH domains. The three copies of the SLH domain from separate protein chains come together to form three likely identical ligand-binding sites, whereas previously characterised triple SLH domains are encoded in a single chain and their ligand-binding grooves have different affinities for SCWPs due to differences in binding motif residues in each SLH repeat[40,42,60,61]. The functional consequences of having equivalent or non-equivalent ligand binding sites are not clear in the context of a protein anchoring to the PG/SCWP.

SlpA from *D. radiodurans* is the only other OmpM-like protein for which structures have been so far available[29,30]. SlpA, like VpOmpM1, plays an important role in maintaining cell envelope integrity[16,31]. VpOmpM1 is similar to SlpA only in its overall architecture: both proteins are trimers and have an N-terminal SLH domain connected via a coiled-coil to a C-terminal β-barrel domain. However, the VpOmpM1 β-barrel trimer is approximately the size of a single SlpA β-barrel (Supplementary Figure 12). Consequently, the pore inside the SlpA β-barrel, although constricted by extracellular loop insertions, is much larger than in VpOmpM1 and is ~14 Å in diameter at the narrowest point. VpOmM1 clearly imposes a size filter for diffusion across the OM (Figure 5) and prevents leakage of large periplasmic contents outside the cell. SlpA has been shown to transport nutrients[30], but it is unclear how escape of periplasmic material via the massive SlpA β-barrel pore is prevented *in vivo*. Other components of the complex and unusual cell envelope of *D. radiodurans* could partially obstruct the SlpA pore[32,33]. A β-sandwich protein (DR_0644) was observed bound at the top of the stalk and the β-barrel interface in one SlpA structure[29], and there are no homologues of this protein present in the *V. parvula* genome. The authors of one study note that

519 large (28-30 strand) β-barrels in OmpM-like proteins could be confined to the
520 Deinococcus-Thermus phylum[29], thus, the unusual β-barrel structure of SlpA and the
521 partner protein DR_0644 might be adaptations to extreme environments in which
522 members of this phylum are found. VpOmpM1, on the other hand, could be more
523 representative of OmpM proteins in mesophilic diderm Terrabacteria.
524
525 The β-barrel of Mep45, the OmpM homologue from *S. ruminantium*, has been shown
526 to form a diffusion channel with similar properties to VpOmpM1, albeit with a larger
527 estimated diameter (11.6 Å) than VpOmpM1 (7.4 Å)[19]. Cyanobacterial OmpM
528 homologues have been shown to form small channels that facilitate transport of
529 inorganic ions[20]. Our VpOmpM1 structures suggest that OmpM homologues from
530 these and perhaps most diderm Terrabacteria might be similar to proteobacterial
531 porins, unlike *D. radiodurans* SlpA. Structural similarity to evolutionarily distant porins
532 supports the hypothesis that OmpM is an ancestral OM tethering system that may
533 have been present in the last common bacterial ancestor[16].
534
535 Our results show that nutrient acquisition and OM tethering are genetically linked via
536 OmpM in *V. parvula* and likely in all Negativicutes and other diderm Terrabacteria. We
537 support the hypothesis that deletion of or mutations in *ompM* promoted loss of the
538 OM[16,62] and extend it by proposing that it was due to the concurrent loss of two key
539 OM-related functions, tethering and nutrient uptake. Although we envisage that OmpM
540 plays similar roles in all diderm Terrabacteria, experimental characterisation of OmpM
541 orthologues from diverse organisms will be required to fully capture the conservation
542 and variation of this ancient OM tether system.
543

544 **Methods**

Bacterial strains, culture conditions and strain manipulation

Bacterial strains used in this work are listed in Supplementary Table 3. *E. coli* strains were genetically manipulated using standard laboratory procedures[63]. When needed, the following compounds were added to *E. coli* cultures at the following concentrations: ampicillin (liquid media) or ticarcillin (solid media) – 100 mg/l, chloramphenicol – 30 mg/l (liquid media) or 25 mg/l (solid media), kanamycin – 50 mg/ml, apramycin – 50 mg/l, diaminopimelic acid – 300 µM.

V. parvula was manipulated as described previously[16,64,65]. When needed, the following compounds were added to *V. parvula* cultures at the following concentrations: chloramphenicol – 25 mg/l, anhydrotetracycline – 250 µg/l. The anaerobic conditions were generated using the GenBag Anaer generator (Biomérieux), or the GP Campus anaerobic chamber (Jacomex). The anaerobic chamber was filled with a $H_2/CO_2/N_2$ (5%/5%/90%) mixture.

Plasmids, primers, and DNA manipulation

All plasmids and primers used in this study are listed in Supplementary Tables 4 and 5, respectively. Cloning was performed using either NEBuilder HiFi DNA Assembly Master Mix (New England Biolabs) or standard restriction cloning methods. Chemically competent homemade *E. coli* DH5α or TOP10 cells[66] were used for transformation of cloning products or plasmids. *V. parvula* genomic DNA was extracted according to a protocol previously described for *Streptomyces* gDNA extraction[67] from stationary phase cultures in SK medium[68]. PCR reactions for cloning applications were carried out using Phusion HiFi Master Mix (Thermo Fisher Scientific) according to manufacturer's protocol. PCR reactions for the control of constructs were carried out using the DreamTaq Green MasterMix (Thermo Fisher Scientific) or the

EmeraldAmp GT PCR Master Mix (Takara Bio). Primers were obtained from Merck or Eurofins Genomics. PCR products were purified using the NucleoSpin Gel and PCR Clean-up kit (Macherey-Nagel). Restriction enzymes were of the FastDigest family of products (Thermo Fisher Scientific). Digestion products were isolated on agarose gels and purified with the NucleoSpin Gel and PCR Clean-up kit (Macherey-Nagel). Plasmid isolation was performed with NucleoSpin Plasmid kit (Macherey-Nagel). Sequence in silico manipulation was carried out using SnapGene (GSL Biotech, www.snapgene.com) and Geneious (Dotmatics). Primers were designed with NEBuilder (New England Biolabs, nebuilder.neb.com). Construct Sanger sequencing was performed by Eurofins (eurofinsgenomics.eu).

Construction of expression vectors

For full length VpOmpM1 expression in *E. coli* we inserted the VpOmpM1 CDS without the signal peptide into the pB22 vector (adding *E. coli* TamB signal peptide and seven histidine residues to the N-terminus). Briefly, we amplified the VpOmpM1 fragment with the JW203/JW202 primer pair using *V. parvula* SKV38 gDNA as a template and cloned it into pB22 digested with XhoI/XbaI, yielding the pJW46 vector. Similarly, the β-barrel portion of VpOmpM1 (pJW45) and FNLLGLLA_00518 (pB22-00518_21-200**)**, and full-length FNLLGLLA_00833 (pB22-00833) were cloned into pB22. The *ompM1* region coding for the stalk (residues 22-107) was amplified from *V. parvula* SKV38 gDNA with the primer pair stalk_F/R, digested with NcoI and XhoI, and cloned into pET28b yielding a C-terminal His_6 fusion. For the expression of full length VpOmpM1 in *V. parvula,* we inserted the C-terminally His-tagged *ompM1* coding gene containing the native ribosome binding site into pRPF185 using the JW172/JW206 primer pair and *V. parvula* SKV38 gDNA as a template, yielding vector pJW48. The vector was

596 then transferred by conjugation into the Δ*ompM1-3 V. parvula* mutant strain as
597 described previously (Witwinowski *et al.* 2022).
598
599 **Protein expression and purification in *E. coli***
600 *E. coli* C43(DE3) Δ*cyoABCD* (Cyo complex deletion to improve purity) cells were
601 transformed with a pB22 plasmid carrying either the full-length VpOmpM1 (pJW46),
602 barrel-only VpOmpM1 (pJW45), barrel-only FNLLGLLA_00518 (pB22-00518_21-200)
603 or full-length FNLLGLLA_00833 (pB22-00833). After overnight incubation at 37°C,
604 transformants were picked from Lysogeny Broth (LB)-ampicillin plates and used to
605 inoculate a starter LB-ampicillin culture incubated at 37°C with shaking for 2 h. Flasks
606 with 1 l LB were inoculated with 8-12 ml of the starter culture and incubated at 37°C,
607 160 rpm until OD600~0.5-0.6. Protein expression was induced by supplementing the
608 cultures with 0.1% arabinose, followed by a further 3-4 h incubation at 37°C with
609 shaking. Cultures were harvested and cell pellets were stored at -20°C.
610 Cell pellets were thawed, resuspended in cold 20 mM Tris-HCl pH 8.0, 300 mM NaCl
611 (TBS) and supplemented with DNase I. Cells were lysed by passing the cell
612 suspension once through a cell disruptor (Constant Systems) at 23 kpsi. The lysate
613 was clarified by centrifugation at 30,000g, 4°C for 30 min. The membranes were
614 isolated from the clarified lysate by ultracentrifugation at 42,000 rpm (45 Ti rotor,
615 Beckman), 4°C for 50 min. The membranes were solubilised in 2.5% Elugent
616 (Millipore) in TBS for 1 h at 4°C. Insoluble material was pelleted by centrifugation at
617 44,000g, 4°C for 30 min. The solubilised fraction was passed through a ~4 ml chelating
618 sepharose column charged with Ni^{2+} ions. The column was washed with 20 column
619 volumes of TBS with 30 mM imidazole and 0.15% lauryldimethylamine oxide (LDAO),
620 and bound protein was eluted with TBS supplemented with 200 mM imidazole and
621 0.2% decyl maltoside (DM). The eluate was concentrated using an Amicon Ultra

filtration device (50 kDa cut-off membrane), loaded on a HiLoad Superdex 200 16/60 column and eluted in 10 mM HEPES-NaOH pH 7.5, 100 mM NaCl, 0.12% DM. Fractions were analysed by SDS-PAGE, pooled, concentrated by filtration (100 kDa cut-off membrane) and flash-frozen in liquid nitrogen. Protein samples were stored at -80°C.

E. coli BL21 (DE3) cells were transformed with the pET28b-SLH_22-107 plasmid for production of the VpOmpM1 stalk region. Expression cultures were set up as above, except kanamycin instead of ampicillin was used in all media, and protein expression was induced by adding 0.4 mM isopropyl β-D-1-thiogalactopyranoside instead of arabinose. Protein purification was performed as above, omitting the ultracentrifugation and solubilisation steps, and without detergents in buffers. A 10 kDa cut-off membrane was used for concentrating protein.

E. coli BL21 (DE3) cells were transformed with the pBAD24-EcOmpF plasmid for production of EcOmpF. Protein expression and purification was performed as for the pB22 constructs up to the membrane isolation stage. Inner membranes were selectively solubilised in 20 mM HEPES-NaOH pH 7.5 and 0.5 % (w/v) sodium lauroyl sarcosinate for 30 min at room temperature with stirring. The insoluble fraction containing the outer membranes was recovered by ultracentrifugation for 30 min at 42,000 rpm (45 Ti rotor). The sarcosinate wash and ultracentrifugation steps were repeated once. Outer membranes were solubilised in 20 mM HEPES-NaOH pH 7.5, 50 mM NaCl and 1.5% LDAO for 1 h at 4°C. The extract was clarified by ultracentrifugation and loaded on a 1 ml ResourceQ anion exchange column (Cytiva). The column was washed and eluted with a 0-500 mM NaCl gradient. Fractions containing EcOmpF were concentrated and subjected to size exclusion chromatography on a Superdex200 10/300 GL column (10 mM HEPES-NaOH pH 7.5,

100 mM NaCl, 0.05% LDAO). The protein was further purified on a MonoQ 5/50 GL anion exchange column (Cytiva), and detergent was exchanged to 0.12% DM via a final size exclusion chromatography run.

Expression and purification of VpOmpM1 from *V. parvula*

15 l of *V. parvula* was grown overnight in anaerobic SK media containing 1.2% sodium lactate and supplemented with 700 µg/l sodium resazurin as an oxygen indicator. Briefly, media was mixed from sterile components, boiled to remove oxygen from the solution (until resazurin appeared colourless) and flushed for 15 minutes with N_2 to remove oxygen from the bottle head volume, before being sealed with a pierceable lid. Anaerobic bottles were inoculated from overnight starter cultures at an OD of 0.04 and supplemented with 25 mg/l chloramphenicol and 250 µg/l anhydrotetracycline. Cultures were grown at 37°C overnight with 180 rpm agitation. Cells were harvested by centrifugation 8000 g for 10 minutes. Pellets were pooled to represent 1.5 l of original culture each and resuspended in 5 ml HEPES pH 7.4. 100 µl $3.5x10^4$ U/ml benzonase and a small spatula of lysozyme was added and sample was incubated on ice for 15 minutes. Cells were lysed by two rounds of French press and the debris was pelleted by centrifugation for 90 minutes at 15,000 g. The supernatant was carefully transferred to an ultracentrifuge tube containing 2 ml of a 50% sucrose cushion and centrifuged for 4 hours at 35,000 g. The volume at the Sucrose supernatant interface was extracted, resuspended in 20 ml of HEPES pH 7.4 and pelleted at 35,000 g for 4 hours. Pelleted membranes were frozen in liquid nitrogen and stored at -80ºC.

V. parvula membrane solubilization and the protein purification procedure was the same as for VpOmpM1 expressed in *E. coli*, except that the flow-through from the chelating sepharose column was put through the column again due to poor binding of

674 protein of interest to the resin. The final size exclusion chromatography step was done
675 on a Superdex 200 10/300 Increase column.
676
677 **Cryo-EM structure determination**
678 Purified VpOmpM1 from *E. coli* (11.6 mg/ml) or *V. parvula* (8 mg/ml) was applied to
679 glow discharged Quantifoil 1.2/1.3 200 mesh holey carbon grids. The grids were
680 immediately blotted and plunge-frozen in liquid ethane using a Vitrobot Mark IV
681 (ThermoFisher Scientific) device operating at 4˚C and 100% humidity. Data were
682 collected on a FEI Glacios microscope operating at 200 kV using a Falcon 4 direct
683 electron detector (ThermoFisher Scientific) at the University of York (Supplementary
684 Table 1). A total of 4,284 and 6,505 movies with the *E. coli* and *V. parvula* samples,
685 respectively, were recorded in electron event representation (EER) mode at 240,000
686 magnification, corresponding to a pixel size of 0.574 Å.
687
688 All image processing was done in cryoSPARC v3.3.2[69,70]. Movies were motion
689 corrected using patch motion correction, and CTF parameters were estimated using
690 patch CTF estimation. For VpOmpM1 expressed in *E. coli,* 2D classes generated from
691 manually picked particles were used for template-based picking. 838,051 particles
692 were extracted in 600 pixel boxes and Fourier cropped to 300 pixel boxes
693 corresponding to a pixel size of 1.148 Å. Three rounds of 2D classification were used
694 to discard bad particles, followed by generation of an ab initio 3D map using a
695 stochastic gradient descent algorithm with 3 classes and 145,518 particles. All three
696 classes were very similar, and a single class was used as a template in non-uniform
697 refinement with the whole particle stack either without symmetry (C1) or with C3
698 symmetry enforced, with per-particle defocus and CTF group parameter (beam tilt and
699 trefoil) refinement enabled. The 145,518 particle stack was subjected to

heterogeneous refinements against the C1 map from non-uniform refinement and three decoy templates, or against the C3 map and the same three decoy templates. Particles were re-extracted in 600 pixel boxes with a pixel size of 0.574 Å. The final particle stacks (96,280 particles for the C1 map; 119,001 particles for the C3 map) were subjected to non-uniform refinement either with C1 or C3 symmetry enforced. The native VpOmpM1 dataset was processed similarly, except that two rounds of 2D classification were performed, four classes were used to make the ab initio map, four decoy templates were used in heterogeneous refinement, and the pixel size remained 1.148 Å throughout.

The final B-factor-sharpened maps from non-uniform refinement were used to build the models. A de novo model was built into the C3 map using Buccaneer[71], followed by cycles of manual building in COOT[72] and real space refinement in Phenix[73]. The C3 model was then docked into the C1 map, manually extended in COOT and real-space-refined. The model built into the C1 map of VpOmpM1 expressed in *E. coli* was docked into the native VpOmpM1 C1 map, manually adjusted in COOT and real-space-refined.

Crystal structure determination

The purified VpOmpM1 stalk construct was concentrated to ~20 mg/ml. Sitting drop vapour diffusion crystallisation screens were set up using a Mosquito robot (SPT Labtech). Crystals grew in 0.1 M citric acid pH 3.5, 2.0 M ammonium sulphate at 20˚C. Crystals were cryo-protected in mother liquor supplemented with ~20% PEG400 and flash-cooled in liquid nitrogen. Diffraction data were collected at the synchrotron beamline I03 at Diamond Light Source (UK) at a temperature of 100 K (Supplementary Table 2). The dataset was processed with XIA2[74], scaled with Aimless[75], and the

space group was confirmed with Pointless[76]. Data quality was evaluated in Xtriage[73]. Arcimboldo[77], part of the CCP4i2 suite[78], was used for ab initio phasing. The initial model was extended by Buccaneer and subjected to cycles of manual building and refinement in Phenix[73] (Supplementary Table 2).

Computational Modelling & Simulation

VpOmpM1 model building. Computational models of trimeric full-length VpOmpM1 were predicted using AlphaFold2[37]. Two unique structures were predicted: one with an extended coiled-coil stalk, and one with a compacted stalk region (Supplementary Figure 4). The AlphaFold2 predicted structure with the extended stalk displays no tilt of the stalk relative to the z-axis, in contrast to the reconstructed cryo-EM density. To generate a full-length VpOmpM1 structure with a tilted stalk consistent with the experimental data, the extended stalk of the AlphaFold2 prediction was fit into the low resolution cryo-EM density and grafted to the well-resolved experimental structure using ChimeraX[79].

System generation. Three different models of VpOmpM1 were used to build protein-membrane systems: full-length VpOmpM1 with the grafted extended stalk; full-length VpOmpM1 with the compacted stalk (AlphaFold2 predicted structure); and truncated VpOmpM1 from the reconstructed cryo-EM density (from residue L100 onwards). For each protein model, the β-barrel domain of the VpOmpM1 trimer was embedded in a model *Escherichia coli* outer membrane using the CHARMM-GUI Membrane Builder module[80]. The inner leaflet consisted of 90% 1-palmitoyl-2-oleoyl-sn-glycero-3-phosphoethanolamine (POPE), 5% 1-palmitoyl-2-oleoyl-sn-glycero-3-phosphoglycerol (POPG), and 5% 1',3'-bis[1-palmitoyl-2-oleoyl-sn-glycero-3-phospho]glycerol (cardiolipin), and the outer leaflet consisted of 100% LPS (R1 core,

752 5 x O1 O-antigen units). This asymmetric bilayer system was solvated in 150 mM KCl,
753 with additional calcium ions to neutralise the LPS headgroups (~115 mM in each
754 system).
755
756 **Atomistic Molecular Dynamics Simulations.** All simulations used the
757 CHARMM36m forcefield[81] with the TIP3P water model[82]. Simulations were carried out
758 using the GROMACS simulation package (version 2021.2)[83]. For all simulation steps,
759 a cut-off of 1.2 nm was applied to Lennard-Jones interactions and short-range
760 electrostatics using the potential shift Verlet scheme. Long-range electrostatics were
761 treated using the particle mesh-Ewald (PME) method[84]. Atoms were constrained using
762 the LINCS algorithm to allow the use of a 2 fs timestep in NPT equilibration and
763 production phases[85]. The three systems were energy minimised in 5000 steps using
764 the steepest descent method[86]. The subsequent systems were equilibrated in six
765 phases (two NVT and four NPT phases) in which the protein and lipid headgroups
766 were subjected to position restraints with varying force constants (Supplementary
767 Table 6). All equilibration phases used the Berendsen thermostat[87] to bring the system
768 to 303.15 K (coupling constant of 1.0 ps). NPT equilibration phases used semi-
769 isotropic Berendsen pressure coupling scheme[87] to equilibrate with a pressure bath of
770 1 bar (τp = 5.0 ps, compressibility of 4.5×10^{-5} bar^{-1}).
771
772 These equilibrated systems were then simulated. The extended stalk system was
773 simulated in duplicate for 1 μs, and the compacted and truncated stalk systems were
774 each simulated as a single replicate for 1 μs. These production simulations utilised the
775 Nosé-Hoover thermostat[88] (coupling constant of 1.0 ps) and the semi-isotropic
776 Parrinello-Rahman barostat[89] (τp = 5.0 ps, compressibility of 4.5×10^{-5} bar^{-1}).
777 Trajectories were analysed using GROMACS tools and MDAnalysis utilities[90,91].

Molecular graphics and supplementary animations were generated using VMD (version 1.9.4a51)[92] and Molywood (version 0.22)[93].

Bilayer electrophysiology

Electrophysiology measurements were carried out in a custom-made cuvette at the centre of which was suspended a 25 μm thick Teflon film (Goodfellow Cambridge Ltd) with a 80-100 μm aperture and 1.25 ml electrode chambers either side of the film. The Teflon film aperture was made lipophilic by 'painting' with 1.5-3 μl 1% hexadecane in hexane solution on both sides, and the hexane was allowed to evaporate for at least 30 min. Electrophysiology buffer (10 mM HEPES-KOH pH 7.5, 1 M KCl) was added to both cuvette chambers, and 3 μl of 5 mg/ml 1,2-diphytanoyl-sn-glycero-3-phosphocholine (DPhPC) dissolved in *n*-pentane was added. The *n*-pentane was left to evaporate for at least 5 min. DPhPC bilayers were formed using the method of Montal and Mueller[94]. Pure, concentrated protein (7-15 mg/ml) was serially diluted in 1% Genapol X-100 (Sigma). 0.3-0.5 μl of diluted protein was added to the *cis* (ground side) chamber, and diluted with electrophysiology buffer as required to promote protein insertion into the bilayer. Protein insertion events were detected as sudden jumps in current in constant-voltage mode. All measurements were carried out using Ag/AgCl pellet electrodes attached to an Axopatch 200B amplifier headstage, and a Digidata 1440A digitiser. The cuvette and headstage were enclosed in a custom-made Faraday shield during recording. Clampex software was used for recording. Clampfit software was used to analyse data.

Liposome swelling assays

Liposome swelling assays were carried out using the method of Nikaido and Rosenberg[95] with modifications. Lipid solution (4 mg/ml phosphatidylcholine and 0.46

mg/ml dihexadecyl phosphate in chloroform) was dried under an air stream, and completely dried under vacuum for at least 2 h. 80 μl of lipid solution was used per condition, *i.e.* per protein to be reconstituted. The dried lipids were resuspended in 100 μl deionised water per condition. Equimolar amounts of protein were added to the resuspended lipid so that the total protein quantity was 15-30 μg, followed by immediate vortexing. All conditions were supplemented with DM containing buffer to ensure that equal amounts of detergent were present in all samples. DM containing buffer was added to control liposomes. Solutions were sonicated in a water bath for 1-1.5 min until translucent, and dried under vacuum overnight. The following day the proteoliposomes were rehydrated in 200 μl 10 mM HEPES-NaOH pH 7.5 and 12 mM stachyose per condition for 1-2 h at room temperature. Control liposomes were used to determine the concentration of each substrate that is isosmotic to the intraliposomal milieu (i.e. there is no swelling of the control liposomes), usually between 7.5 and 15 mM substrate in 10 mM HEPES-NaOH pH 7.5. Substrate concentrations used can be found in Supplementary Table 7. The decrease in A_{400} due to liposome swelling was measured after adding 200 μl of the substrate solution to 15 μl of the proteoliposome suspension. Readings were taken on a Perkin Elmer Lambda 35 spectrophotometer in 1 s intervals for 30 s. A line was fit to the absorbance data corresponding to the linear phase of swelling (2-15 s), and the slope of the line was recorded as the swelling rate. Control liposome swelling rates were subtracted from all proteoliposome swelling rates. All data were normalized to EcOmpF-containing liposome swelling in the presence of arabinose.

Data availability

828 Electron microscopy maps have been deposited in the Electron Microscopy Data Bank
829 with the accession codes EMD-16328 (VpOmpM1 from *E. coli* in C1), EMD-16333
830 (VpOmpM1 from *E. coli* in C3) and EMD-16332 (VpOmpM1 from *V. parvula* in C1).
831 Models built into the cryo-EM maps have been deposited in the Protein Data Bank
832 under accession codes 8BYM (VpOmpM1 from *E. coli* in C1), 8BYT (VpOmpM1 from
833 *E. coli* in C3) and 8BYS (VpOmpM1 from *V. parvula* in C1). The structure factors and
834 atomic coordinates for the VpOmpM1 stalk crystal structure have been deposited in
835 the Protein Data Bank under accession code 8BZ2. Other data presented in this paper,
836 constructs and strains are available on reasonable request.
837

838 ## Acknowledgements

839 We thank the University of York (UK) electron cryo-microscopy facility for access to
840 instrumentation and support. We acknowledge the Diamond Light Source for I03
841 beamline access (proposal mx-24948) and support. We thank Arnaud Baslé for
842 collecting X-ray data, maintaining the Newcastle Structural Biology Laboratory, and
843 computing support. We thank David Staunton (University of Oxford) for carrying out
844 the dynamic scanning calorimetry experiments. This work was supported by a
845 Wellcome Trust Investigator award (214222/Z/18/Z) to B.v.d.B., providing salary
846 support to A.S. and Y.Z. C.B., S.G., J.W., and R.E.S. were supported by funding from
847 the French National Research Agency (ANR) (no. Fir-OM ANR-16-CE12-0010), the
848 Institut Pasteur Programmes Transversaux de Recherche (no. PTR 39-16), and the
849 French government Investissement d'Avenir Program, Laboratoire d'Excellence
850 Integrative Biology of Emerging Infectious Diseases (grant no. ANR-10-LABX-62-
851 IBEID). We acknowledge the use of the IRIDIS High Performance Computing Facility,
852 and associated support services at the University of Southampton, in the completion
853 of this work. K.E.N. was supported by a Ph.D. Studentship from the Engineering and

Physical Sciences Research Council (Project Number: 2446840), and S.K. by an EPSRC established Career Fellowship (EPSRC grant no. EP/V030779/1).

Author contributions

A.S. made constructs, purified proteins, determined cryo-EM and crystal structures, carried out functional assays, and wrote the manuscript with input from all authors. Y.Z. purified proteins and carried out functional assays. K.E.N. performed simulations, supervised by S.K. J.W. made constructs and strains and prepared the dataset for ConSurf analysis. R.E.S. grew *V. parvula*, prepared membrane pellets, and isolated sacculi. S.P.B. collected preliminary electrophysiology data. A.B. collected X-ray diffraction data and managed the Newcastle Structural Biology Laboratory. B.v.d.B. made constructs, purified and crystallised proteins. S.G., C.B. and B.v.d.B. conceived and supervised the project.

Ethics declarations

The authors declare no competing interests.

References

1. Silhavy, T. J., Ruiz, N. & Kahne, D. Advances in understanding bacterial outer-membrane biogenesis. *Nat. Rev. Microbiol. 2006 41* **4**, 57–66 (2006).
2. Sun, J., Rutherford, S. T., Silhavy, T. J. & Huang, K. C. Physical properties of the bacterial outer membrane. *Nat. Rev. Microbiol.* **20**, 236–248 (2022).
3. Bladen, H. A. & Mergenhagen, S. E. Ultrastructure of *Veillonella* and morphological correlation of an outer membrane with particles associated with endotoxic activity. *J. Bacteriol.* **88**, 1482 (1964).
4. Rojas, E. R. *et al.* The outer membrane is an essential load-bearing element in Gram-negative bacteria. *Nature* **559**, 617–621 (2018).
5. Braun, V. & Rehn, K. Chemical Characterization, Spatial Distribution and Function of a Lipoprotein (Murein-Lipoprotein) of the *E. coli* Cell Wall. *Eur. J. Biochem.* **10**, 426–438 (1969).
6. Braun, V. Covalent lipoprotein from the outer membrane of *Escherichia coli*. *Biochim. Biophys. Acta - Rev. Biomembr.* **415**, 335–377 (1975).
7. Cascales, E., Bernadac, A., Gavioli, M., Lazzaroni, J. C. & Lloubes, R. Pal

lipoprotein of *Escherichia coli* plays a major role in outer membrane integrity. *J. Bacteriol.* **184**, 754–759 (2002).

8. Bouveret, E., Bénédetti, H., Rigal, A., Loret, E. & Lazdunski, C. In vitro characterization of peptidoglycan-associated lipoprotein (PAL)- peptidoglycan and PAL-TolB interactions. *J. Bacteriol.* **181**, 6306–6311 (1999).
9. Parsons, L. M., Lin, F. & Orban, J. Peptidoglycan recognition by Pal, an outer membrane lipoprotein. *Biochemistry* **45**, 2122–2128 (2006).
10. Park, J. S. *et al.* Mechanism of anchoring of OmpA protein to the cell wall peptidoglycan of the gram-negative bacterial outer membrane. *FASEB J.* **26**, 219–228 (2012).
11. Samsudin, F., Boags, A., Piggot, T. J. & Khalid, S. Braun's Lipoprotein Facilitates OmpA Interaction with the *Escherichia coli* Cell Wall. *Biophys. J.* **113**, 1496–1504 (2017).
12. Sonntag, I., Schwarz, H., Hirota, Y. & Henning, U. Cell envelope and shape of *Escherichia coli*: multiple mutants missing the outer membrane lipoprotein and other major outer membrane proteins. *J. Bacteriol.* **136**, 280 (1978).
13. Suzuki, H. *et al.* Murein-lipoprotein of *Escherichia coli*: a protein involved in the stabilization of bacterial cell envelope. *Mol. Gen. Genet.* **167**, 1–9 (1978).
14. Bernadac, A., Gavioli, M., Lazzaroni, J. C., Raina, S. & Lloubès, R. *Escherichia coli tol-pal* mutants form outer membrane vesicles. *J. Bacteriol.* **180**, 4872–4878 (1998).
15. Wang, Y. The Function of OmpA in *Escherichia coli*. *Biochem. Biophys. Res. Commun.* **292**, 396–401 (2002).
16. Witwinowski, J. *et al.* An ancient divide in outer membrane tethering systems in bacteria suggests a mechanism for the diderm-to-monoderm transition. *Nat. Microbiol.* **7**, 411–422 (2022).
17. Kalmokoff, M. L. *et al.* Physical and genetic characterization of an outer-membrane protein (OmpM1) containing an N-terminal S-layer-like homology domain from the phylogenetically Gram-positive gut anaerobe *Mitsuokella multacida*. *Anaerobe* **15**, 74–81 (2009).
18. Kojima, S. *et al.* Cadaverine covalently linked to peptidoglycan is required for interaction between the peptidoglycan and the periplasm-exposed S-layer-homologous domain of major outer membrane protein Mep45 in *Selenomonas ruminantium*. *J. Bacteriol.* **192**, 5953–5961 (2010).
19. Kojima, S. *et al.* Peptidoglycan-associated outer membrane protein Mep45 of rumen anaerobe *Selenomonas ruminantium* forms a non-specific diffusion pore via its C-terminal transmembrane domain. *Biosci. Biotechnol. Biochem.* **80**, 1954 (2016).
20. Kowata, H., Tochigi, S., Takahashi, H. & Kojima, S. Outer Membrane Permeability of Cyanobacterium *Synechocystis* sp. Strain PCC 6803: Studies of Passive Diffusion of Small Organic Nutrients Reveal the Absence of Classical Porins and Intrinsically Low Permeability. *J. Bacteriol.* **199**, (2017).
21. Olabarría, C., Carrascosa, J. L., De Pedro, M. A. & Berenguer, J. A conserved motif in S-layer proteins is involved in peptidoglycan binding in *Thermus thermophilus*. *J. Bacteriol.* **178**, 4765 (1996).
22. Cava, F., De Pedro, M. A., Schwarz, H., Henne, A. & Berenguer, J. Binding to pyruvylated compounds as an ancestral mechanism to anchor the outer envelope in primitive bacteria. *Mol. Microbiol.* **52**, 677–690 (2004).
23. Kojima, S. & Okumura, Y. Outer membrane-deprived cyanobacteria liberate periplasmic and thylakoid luminal components that support the growth of heterotrophs. *bioRxiv* 2020.03.24.006684 (2020). doi:10.1101/2020.03.24.006684

24. Kamio, Y., Itoh, Y. & Terawaki, Y. Chemical structure of peptidoglycan in *Selenomonas ruminantium*: Cadaverine links covalently to the D-glutamic acid residue of peptidoglycan. *J. Bacteriol.* **146**, 49–53 (1981).
25. Kamio, Y. & Nakamura, K. Putrescine and cadaverine are constituents of peptidoglycan in *Veillonella alcalescens* and *Veillonella parvula*. *J. Bacteriol.* **169**, 2881–2884 (1987).
26. Nikaido, H. & Vaara, M. Molecular basis of bacterial outer membrane permeability. *Microbiol. Rev.* **49**, 1 (1985).
27. Nikaido, H. Molecular basis of bacterial outer membrane permeability revisited. *Microbiol. Mol. Biol. Rev.* **67**, 593–656 (2003).
28. Poppleton, D. I. *et al.* Outer Membrane Proteome of *Veillonella parvula*: A Diderm Firmicute of the Human Microbiome. *Front. Microbiol.* **8**, (2017).
29. von Kügelgen, A., van Dorst, S., Alva, V. & Bharat, T. A. M. A multidomain connector links the outer membrane and cell wall in phylogenetically deep-branching bacteria. *Proc. Natl. Acad. Sci. U. S. A.* **119**, e2203156119 (2022).
30. Farci, D. *et al.* The cryo-EM structure of the S-layer deinoxanthin-binding complex of *Deinococcus radiodurans* informs properties of its environmental interactions. *J. Biol. Chem.* **298**, (2022).
31. Rothfuss, H., Lara, J. C., Schmid, A. K. & Lidstrom, M. E. Involvement of the S-layer proteins Hpi and SlpA in the maintenance of cell envelope integrity in *Deinococcus radiodurans* R1. *Microbiology* **152**, 2779–2787 (2006).
32. Farci, D., Haniewicz, P. & Piano, D. The structured organization of *Deinococcus radiodurans'* cell envelope. *Proc. Natl. Acad. Sci. U. S. A.* **119**, e2209111119 (2022).
33. von Kügelgen, A. *et al.* Title Interdigitated immunoglobulin arrays form the hyperstable surface layer of the extremophilic bacterium *Deinococcus radiodurans*. *bioRxiv* 2022.09.15.508085 (2022). doi:10.1101/2022.09.15.508085
34. Cowan, S. W. *et al.* Crystal structures explain functional properties of two *E. coli* porins. *Nature* **358**, 727–733 (1992).
35. Baslé, A., Rummel, G., Storici, P., Rosenbusch, J. P. & Schirmer, T. Crystal structure of osmoporin OmpC from *E. coli* at 2.0 A. *J. Mol. Biol.* **362**, 933–942 (2006).
36. Xie, Y. *et al.* IBS 2.0: an upgraded illustrator for the visualization of biological sequences. *Nucleic Acids Res.* **50**, W420–W426 (2022).
37. Jumper, J. *et al.* Highly accurate protein structure prediction with AlphaFold. *Nat. 2021 5967873* **596**, 583–589 (2021).
38. Mesnage, S. *et al.* Bacterial SLH domain proteins are non-covalently anchored to the cell surface via a conserved mechanism involving wall polysaccharide pyruvylation. *EMBO J.* **19**, 4473–4484 (2000).
39. Kern, J. *et al.* Structure of Surface Layer Homology (SLH) Domains from *Bacillus anthracis* Surface Array Protein. *J. Biol. Chem.* **286**, 26042–26049 (2011).
40. Blackler, R. J. *et al.* Structural basis of cell wall anchoring by SLH domains in *Paenibacillus alvei*. *Nat. Commun. 2018 91* **9**, 1–11 (2018).
41. Sychantha, D. *et al.* Molecular Basis for the Attachment of S-Layer Proteins to the Cell Wall of *Bacillus anthracis*. *Biochemistry* **57**, 1949–1953 (2018).
42. Legg, M. S. G. *et al.* The S-layer homology domains of *Paenibacillus alvei* surface protein SpaA bind to cell wall polysaccharide through the terminal monosaccharide residue. *J. Biol. Chem.* **298**, 101745 (2022).
43. Vassylyev, D. G., Tomitori, H., Kashiwagi, K., Morikawa, K. & Igarashi, K. Crystal Structure and Mutational Analysis of the *Escherichia coli* Putrescine

Receptor: STRUCTURAL BASIS FOR SUBSTRATE SPECIFICITY. *J. Biol. Chem.* **273**, 17604–17609 (1998).

44. Wu, D. *et al.* Structural Basis of Substrate Binding Specificity Revealed by the Crystal Structures of Polyamine Receptors SpuD and SpuE from *Pseudomonas aeruginosa*. *J. Mol. Biol.* **416**, 697–712 (2012).
45. Bale, S. *et al.* Structural basis for putrescine activation of human S-adenosylmethionine decarboxylase. *Biochemistry* **47**, 13404–13417 (2008).
46. Sagong, H. Y. *et al.* Crystal Structure and Pyridoxal 5-Phosphate Binding Property of Lysine Decarboxylase from *Selenomonas ruminantium*. *PLoS One* **11**, e0166667 (2016).
47. Kröger, P., Shanmugaratnam, S., Ferruz, N., Schweimer, K. & Höcker, B. A comprehensive binding study illustrates ligand recognition in the periplasmic binding protein PotF. *Structure* **29**, 433-443.e4 (2021).
48. Ashkenazy, H. *et al.* ConSurf 2016: an improved methodology to estimate and visualize evolutionary conservation in macromolecules. *Nucleic Acids Res.* **44**, W344–W350 (2016).
49. Holm, L. Dali server: structural unification of protein families. *Nucleic Acids Res.* **50**, W210–W215 (2022).
50. Karshikoff, A., Spassov, V., Cowan, S. W., Ladenstein, R. & Schirmer, T. Electrostatic Properties of Two Porin Channels from *Escherichia coli*. *J. Mol. Biol.* **240**, 372–384 (1994).
51. Schirmer, T. & Phale, P. S. Brownian dynamics simulation of ion flow through porin channels. *J. Mol. Biol.* **294**, 1159–1167 (1999).
52. Smart, O. S., Neduvelil, J. G., Wang, X., Wallace, B. A. & Sansom, M. S. P. HOLE: A program for the analysis of the pore dimensions of ion channel structural models. *J. Mol. Graph.* **14**, 354–360 (1996).
53. Nestorovich, E. M., Rostovtseva, T. K. & Bezrukov, S. M. Residue Ionization and Ion Transport through OmpF Channels. *Biophys. J.* **85**, 3718–3729 (2003).
54. Schmitt, E. K., Vrouenraets, M. & Steinem, C. Channel activity of OmpF monitored in nano-BLMs. *Biophys. J.* **91**, 2163–2171 (2006).
55. Efremov, R. G. & Sazanov, L. A. Structure of *Escherichia coli* OmpF porin from lipidic mesophase. *J. Struct. Biol.* **178**, 311–318 (2012).
56. Vandeputte-Rutten, L. *et al.* Crystal structure of the outer membrane protease OmpT from *Escherichia coli* suggests a novel catalytic site. *EMBO J.* **20**, 5033–5039 (2001).
57. Eren, E., Murphy, M., Goguen, J. & van den Berg, B. An Active Site Water Network in the Plasminogen Activator Pla from *Yersinia pestis*. *Structure* **18**, 809–818 (2010).
58. Hong, H., Patel, D. R., Tamm, L. K. & Van Den Berg, B. The Outer Membrane Protein OmpW Forms an Eight-stranded β-Barrel with a Hydrophobic Channel. *J. Biol. Chem.* **281**, 7568–7577 (2006).
59. Hong, H., Szabo, G. & Tamm, L. K. Electrostatic couplings in OmpA ion-channel gating suggest a mechanism for pore opening. *Nat. Chem. Biol. 2006 211* **2**, 627–635 (2006).
60. Mader, C., Huber, C., Moll, D., Sleytr, U. B. & Sára, M. Interaction of the Crystalline Bacterial Cell Surface Layer Protein SbsB and the Secondary Cell Wall Polymer of *Geobacillus stearothermophilus* PV72 Assessed by Real-Time Surface Plasmon Resonance Biosensor Technology. *J. Bacteriol.* **186**, 1758–1768 (2004).
61. Janesch, B., Messner, P. & Schäffer, C. Are the surface layer homology domains essential for cell surface display and glycosylation of the S-layer

protein from *Paenibacillus alvei* CCM 2051T? *J. Bacteriol.* **195**, 565–575 (2013).
62. Taib, N. *et al.* Genome-wide analysis of the Firmicutes illuminates the diderm/monoderm transition. *Nat. Ecol. Evol.* **4**, 1661–1672 (2020).
63. Green, M. R. & Sambrook, J. *Molecular Cloning: A Laboratory Manual (Fourth Edition)*. (Cold Spring Harbor Laboratory Press, 2012).
64. Knapp, S. *et al.* Natural Competence Is Common among Clinical Isolates of *Veillonella parvula* and Is Useful for Genetic Manipulation of This Key Member of the Oral Microbiome. *Front. Cell. Infect. Microbiol.* **7**, (2017).
65. Béchon, N. *et al.* Autotransporters Drive Biofilm Formation and Autoaggregation in the Diderm Firmicute *Veillonella parvula*. *J. Bacteriol.* **202**, (2020).
66. Inoue, H., Nojima, H. & Okayama, H. High efficiency transformation of *Escherichia coli* with plasmids. *Gene* **96**, 23–28 (1990).
67. Jacques, I. B. *et al.* Analysis of 51 cyclodipeptide synthases reveals the basis for substrate specificity. *Nat. Chem. Biol. 2015 119* **11**, 721–727 (2015).
68. Knapp, S. *et al.* Natural Competence Is Common among Clinical Isolates of V*eillonella parvula* and Is Useful for Genetic Manipulation of This Key Member of the Oral Microbiome. *Front. Cell. Infect. Microbiol.* **7**, 139 (2017).
69. Punjani, A., Rubinstein, J. L., Fleet, D. J. & Brubaker, M. A. cryoSPARC: algorithms for rapid unsupervised cryo-EM structure determination. *Nat. Methods 2017 143* **14**, 290–296 (2017).
70. Punjani, A., Zhang, H. & Fleet, D. J. Non-uniform refinement: adaptive regularization improves single-particle cryo-EM reconstruction. *Nat. Methods 2020 1712* **17**, 1214–1221 (2020).
71. Hoh, S. W., Burnley, T. & Cowtan, K. Current approaches for automated model building into cryo-EM maps using Buccaneer with CCP-EM. *Acta Crystallogr. Sect. D, Struct. Biol.* **76**, 531–541 (2020).
72. Emsley, P., Lohkamp, B., Scott, W. G. & Cowtan, K. Features and development of Coot. *Acta Crystallogr. D. Biol. Crystallogr.* **66**, 486–501 (2010).
73. Liebschner, D. *et al.* Macromolecular structure determination using X-rays, neutrons and electrons: recent developments in Phenix. *Acta Crystallogr. Sect. D, Struct. Biol.* **75**, 861–877 (2019).
74. Winter, G. Xia2: An expert system for macromolecular crystallography data reduction. *J. Appl. Crystallogr.* **43**, 186–190 (2010).
75. Evans, P. R. & Murshudov, G. N. How good are my data and what is the resolution? *Acta Crystallogr. Sect. D Biol. Crystallogr.* **69**, 1204–1214 (2013).
76. Evans, P. Scaling and assessment of data quality. in *Acta Crystallographica Section D: Biological Crystallography* **62**, 72–82 (International Union of Crystallography, 2006).
77. Rodríguez, D. D. *et al.* Crystallographic ab initio protein structure solution below atomic resolution. *Nat. Methods 2009 69* **6**, 651–653 (2009).
78. Potterton, L. *et al.* CCP4i2: the new graphical user interface to the CCP4 program suite. *Acta Crystallogr. Sect. D, Struct. Biol.* **74**, 68 (2018).
79. Pettersen, E. F. *et al.* UCSF ChimeraX: Structure visualization for researchers, educators, and developers. *Protein Sci.* **30**, 70–82 (2021).
80. Lee, J. *et al.* CHARMM-GUI Membrane Builder for Complex Biological Membrane Simulations with Glycolipids and Lipoglycans. *J. Chem. Theory Comput.* **15**, 775–786 (2019).
81. Huang, J. & Mackerell, A. D. CHARMM36 all-atom additive protein force field: Validation based on comparison to NMR data. *J. Comput. Chem.* **34**, 2135–

2145 (2013).
82. Jorgensen, W. L., Chandrasekhar, J., Madura, J. D., Impey, R. W. & Klein, M. L. Comparison of simple potential functions for simulating liquid water. *J. Chem. Phys.* **79**, 926 (1998).
83. Van Der Spoel, D. *et al.* GROMACS: Fast, flexible, and free. *Journal of Computational Chemistry* **26**, 1701–1718 (2005).
84. Essmann, U. *et al.* A smooth particle mesh Ewald method. *J. Chem. Phys.* **103**, 8577–8593 (1995).
85. Hess, B., Bekker, H., Berendsen, H. J. C. & Fraaije, J. G. E. M. LINCS: A Linear Constraint Solver for molecular simulations. *J. Comput. Chem.* **18**, 1463–1472 (1997).
86. Goldstein, A. A. On Steepest Descent. *J. Soc. Ind. Appl. Math. Ser. A Control* **3**, 147–151 (1965).
87. Berendsen, H. J. C., Postma, J. P. M., Van Gunsteren, W. F., Dinola, A. & Haak, J. R. Molecular dynamics with coupling to an external bath. *J. Chem. Phys.* **81**, 3684–3690 (1984).
88. Nosé, S. A unified formulation of the constant temperature molecular dynamics methods. *J. Chem. Phys.* **81**, 511–519 (1984).
89. Parrinello, M. & Rahman, A. Polymorphic transitions in single crystals: A new molecular dynamics method. *J. Appl. Phys.* **52**, 7182 (1998).
90. Michaud-Agrawal, N., Denning, E. J., Woolf, T. B. & Beckstein, O. MDAnalysis: A toolkit for the analysis of molecular dynamics simulations. *J. Comput. Chem.* **32**, 2319–2327 (2011).
91. Gowers, R. *et al.* MDAnalysis: A Python Package for the Rapid Analysis of Molecular Dynamics Simulations. in *Proceedings of the 15th Python in Science Conference* 98–105 (SciPy, 2016). doi:10.25080/Majora-629e541a-00e
92. Humphrey, W., Dalke, A. & Schulten, K. VMD: Visual molecular dynamics. *J. Mol. Graph.* **14**, 33–38 (1996).
93. Wieczór, M., Hospital, A., Bayarri, G., Czub, J. & Orozco, M. Molywood: streamlining the design and rendering of molecular movies. *Bioinformatics* **36**, 4660–4661 (2020).
94. Montal, M. & Mueller, P. Formation of Bimolecular Membranes from Lipid Monolayers and a Study of Their Electrical Properties. *Proc. Natl. Acad. Sci. U. S. A.* **69**, 3561 (1972).
95. Nikaido, H. & Rosenberg, E. Y. Porin channels in *Escherichia coli*: studies with liposomes reconstituted from purified proteins. *J. Bacteriol.* **153**, 241–252 (1983).